A discontinuous Galerkin approximation for a wall–bounded consistent three–component Cahn–Hilliard flow model

Juan Manzanero · **Carlos Redondo** ·
Gonzalo Rubio · **Esteban Ferrer** · **Ángel**
Rivero–Jiménez

Abstract We present a high–order discontinuous Galerkin (DG) discretization for the three–phase Cahn–Hilliard model of [Boyer, F., & Lapuerta, C. (2006). Study of a three component Cahn–Hilliard flow model]. In this model, consistency is ensured with an additional term in the chemical free–energy. The model considered in this work includes a wall boundary condition that allows for an arbitrary equilibrium contact angle in three–phase flows. The model is discretized with a high–order discontinuous Galerkin spectral element method that uses the symmetric interior penalty to compute the interface fluxes, and allows for unstructured meshes with curvilinear hexahedral elements. The integration in time uses a first order IMplicit–EXplicit (IMEX) method, such that the associated linear systems are decoupled for the two Cahn–Hilliard equations. Additionally, the Jacobian matrix is constant, and identical for both equations. This allows us to solve the two systems by performing only one LU factorization, with the size of the two–phase system, followed by two Gauss substitutions. Finally, we test numerically the accuracy of the scheme providing convergence analyses for two and three–dimensional cases, including the captive bubble test, the study of two bubbles in contact with a wall and the spinodal decomposition in a cube and in a curved pipe with a "T" junction.

Juan Manzanero (E-mail: juan.manzanero@upm.es), Carlos Redondo, Gonzalo Rubio, Esteban Ferrer,
ETSIAE-UPM - School of Aeronautics, Universidad Politécnica de Madrid. Plaza Cardenal Cisneros 3, E-28040 Madrid, Spain. // Center for Computational Simulation, Universidad Politécnica de Madrid, Campus de Montegancedo, Boadilla del Monte, 28660, Madrid, Spain.
Ángel Rivero-Jiménez
Repsol Technology Lab Agustín de Betancourt S/N, 28935, Móstoles, Madrid, Spain

1 Introduction

The study of multiphase flows is of broad interest for both the scientific community and industrial applications (e.g. oil, gas, and nuclear industries). Multiphase flows study the evolution of two or more immiscible fluids, which tend to segregate and be separated by a thin interface. In this work, we study the dynamics of three dissimilar coexisting phases.

The mathematical modeling of multiphase flows distinguishes two main approaches: the sharp and the diffuse interface methods. On the one hand, the sharp interface method considers an infinitely thin interface, which is tracked using, for example, a level–set method [1, 2]. Then the fluid dynamics equations for each individual phase are solved, being two fluids coupled through an interface condition which enforces mass, momentum, and energy balances [3]. On the other hand, in the diffuse interface (or phase field) methods [4, 5] the interface is regularized and it is provided with a finite, yet thin, thickness. As a result, the concentration of the phases, and all the thermodynamic properties, vary smoothly across the interface.

Among the different diffuse interface methods, the Cahn–Hilliard type models are attracting attention [6, 7, 8, 9, 10, 11, 12, 13, 14, 15]. The Cahn–Hilliard equation integrates the effects of phase separation (segregation) and phase homogenization (mixing) in a free–energy function, which is minimized as the flow evolves. The Cahn–Hilliard model for two phase flows is the simplest, and it has been widely studied in the past [16, 17, 13, 14]. Extending the two phase model to three phases is not immediate, since new physical considerations should be taken into account: the model has to be consistent, i.e., if one of the three phases is not present initially, it can not emerge in further times. Besides, it is desirable that the model reduces to the two–phase Cahn–Hilliard model when one of the phases is not present. In this work, we use the model presented in [18], which solves the consistency problem considering a particular choice of the chemical free–energy. For $N \geqslant 4$ phases, other methods that involve degenerate diffusion coefficients have been developed [10, 19, 20]. The model is augmented with the boundary condition developed in [21], which permits the prescription of the contact angle between the different phases and the wall by solving a non–homogeneous Neumann boundary condition.

The three phase model is numerically approximated in space with a high–order Discontinuous Galerkin Spectral Element Method (DGSEM) [22] that uses the symmetric interior penalty method [23, 24, 25, 26, 27]. The DGSEM

is desirable since it allows arbitrary order of accuracy [28, 22], low dissipative and dispersive errors [29, 30, 31, 32], the representation of arbitrarily three–dimensional complex geometries through the use of unstructured meshes with curvilinear elements [33], efficient mesh adaptation techniques [34, 35, 36], the design of provably stable schemes [37, 38, 39, 40, 13, 41, 14] and it has been used in the past to discretize multiphase (two phase) flows [42, 43, 14]. Other three component Cahn–Hilliard flow models are available and have been discretized by means of the finite element method [44], local discontinuous Galerkin method [45] or spectral element method [10]. The DGSEM has been used by the authors to discretize the two component Cahn–Hilliard flow model [13]. To the authors' knowledge, this is the first implementation of the three component Cahn–Hilliard model of [18] in a discontinuous Galerkin (and in particular a discontinuous Galerkin Spectral Element method) framework. Even though the DGSEM provides us a framework to construct stable schemes, we have not performed a stability analysis here. This is left for future work. Nevertheless, our results suggest a stable formulation that provides a robust solver.

Finally, we consider a first order IMplicit–EXplicit (IMEX) time integrator. We use an IMEX method since the Cahn–Hilliard equation features a linear fourth order spatial operator (which is solved implicitly), and a non–linear second order spatial operator (which is solved explicitly). Therefore the solution of the fully–discrete system involves the solution of one linear system for each of the Cahn–Hilliard equations. The two linear systems, however, are decoupled such that the Jacobian matrices are constant in time and identical for both Cahn–Hilliard equations. This method permits a resolution approach where only one LU factorization is performed for the two equations.

The rest of this work is organized as follows: in Sec. 2 we describe the three component Cahn–Hilliard model. The construction of the discrete DG approximation is described in Sec. 3. Lastly, we provide numerical experiments in Sec. 4 that assess the accuracy of the method. Final conclusions and discussions can be found in Sec. 5.

2 Model description

The phase field approach to multiphase flows introduces one scalar field c_j per fluid, which represents the relative concentration of phase j (i.e. the volume occupied by phase j divided by the total volume) in each space–time point.

The conservation of phases condition, then, reads,

$$\sum_{j=1}^{N_{\text{phases}}} c_j = 1. \tag{1}$$

In this work, we restrict ourselves to three phase flows, $N_{\text{phases}} = 3$.

We detail in this section the three–phase model derived in [18]. As usual in phase field methods, each of the concentration fields is subjected to a Cahn–Hilliard diffusion equation. The Cahn–Hilliard equation is such that the evolution of the concentration minimizes a free–energy. In [18], the free–energy function is,

$$\mathcal{F}_\varepsilon^{[\boldsymbol{\sigma}]}\left(\mathbf{c}, \nabla \mathbf{c}\right) = \int_\Omega \left(\frac{12}{\varepsilon} F_0^{[\boldsymbol{\sigma}]}\left(\mathbf{c}\right) - \frac{3}{8}\varepsilon \left(\nabla \mathbf{c}\right)^T \overline{\overline{\boldsymbol{\sigma}}} \nabla \mathbf{c} \right) \mathrm{d}\mathbf{x}. \tag{2}$$

The free–energy contains two terms. The first term contains the chemical free–energy, $F_0^{[\boldsymbol{\sigma}]}$, which in this model is a polynomial function on the three concentrations $\mathbf{c} = (c_1, c_2, c_3)$. The second term is the interfacial energy, where $\overline{\overline{\boldsymbol{\sigma}}}$ is the interface tension tensor, whose entries are the surface tension coefficients of all the possible interfaces, σ_{ij},

$$\overline{\overline{\boldsymbol{\sigma}}} = \begin{pmatrix} 0 & \sigma_{12} & \sigma_{13} \\ \sigma_{12} & 0 & \sigma_{23} \\ \sigma_{13} & \sigma_{23} & 0 \end{pmatrix}. \tag{3}$$

The interface tension coefficients σ_{ij} are positive constants. Finally, ε is the interface width parameter, which controls the thickness of the diffuse interfaces.

The Cahn–Hilliard equation is constructed such that the concentration time derivatives are proportional to the Laplacian of additional scalar fields called chemical potential, $\boldsymbol{\mu} = (\mu_1, \mu_2, \mu_3)$,

$$c_{j,t} = \frac{M_0}{\Sigma_j} \nabla^2 \mu_j, \quad \Sigma_i = \sigma_{ij} + \sigma_{ik} - \sigma_{jk}, \tag{4}$$

where the positive constant M_0 is called mobility, and Σ_j are constant coefficients called spreading factors. Although in [18] the authors show an extension that allows negative spreading factors, this work only considers positive spreading factors. For the three–phase model, the chemical potentials are defined as,

$$\mu_i = \frac{4\Sigma_T}{\varepsilon} \sum_{\substack{j=1 \\ j \neq i}}^{3} \left(\frac{1}{\Sigma_j} \left[\frac{\partial F_0^{\boldsymbol{\sigma}}}{\partial c_i} - \frac{\partial F_0^{\boldsymbol{\sigma}}}{\partial c_j} \right] \right) - \frac{3}{4}\varepsilon \Sigma_i \nabla^2 c_i, \quad \frac{3}{\Sigma_T} = \frac{1}{\Sigma_1} + \frac{1}{\Sigma_2} + \frac{1}{\Sigma_3}. \tag{5}$$

For simplicity, we define f_i as

$$f_i = \frac{\Sigma_T}{3} \sum_{\substack{j=1 \\ j \neq i}}^{3} \left(\frac{1}{\Sigma_j} \left[\frac{\partial F_0^{\boldsymbol{\sigma}}}{\partial c_i} - \frac{\partial F_0^{\boldsymbol{\sigma}}}{\partial c_j} \right] \right), \quad i = 1, 2, 3, \tag{6}$$

to write the chemical potential as $\mu_i = \frac{12}{\varepsilon} f_i - \frac{3}{4} \varepsilon \Sigma_i \nabla^2 c_i$.

The model is completed with the definition of the chemical free–energy $F_0^{[\boldsymbol{\sigma}]}$. In [18] the chemical free–energy is constructed to satisfy two important properties:

Property 1 *Conservative model. If the initial condition satisfies $c_1(\mathbf{x}, 0) + c_2(\mathbf{x}, 0) + c_3(\mathbf{x}, 0) = 1$, then, for all further times a conservative model maintains*

$$c_1(\mathbf{x}, t) + c_2(\mathbf{x}, t) + c_3(\mathbf{x}, t) = 1, \quad \forall t \geqslant 0. \tag{7}$$

This property is ensured by an appropriate construction of the chemical potentials (5). We sum the three Cahn–Hilliard equations to find that,

$$(c_1 + c_2 + c_3)_t = M_0 \nabla^2 \left(\frac{\mu_1}{\Sigma_1} + \frac{\mu_2}{\Sigma_2} + \frac{\mu_3}{\Sigma_3} \right) = 0. \tag{8}$$

Therefore, it suffices that the chemical potentials satisfy,

$$\frac{\mu_1}{\Sigma_1} + \frac{\mu_2}{\Sigma_2} + \frac{\mu_3}{\Sigma_3} = 0, \tag{9}$$

which they do by construction. The relation (9) allows us to compute the chemical potential of one of the phases (typically the third phase) as a function of the other two phases,

$$\mu_3 = -\frac{\Sigma_3}{\Sigma_1} \mu_1 - \frac{\Sigma_3}{\Sigma_2} \mu_2. \tag{10}$$

Property 2 *Consistent model. If the initial concentrations satisfy $c_j(\mathbf{x}, 0) = 0$, then*

$$c_j(\mathbf{x}, t) = 0, \quad \forall t \geqslant 0. \tag{11}$$

As shown in [18], this property is guaranteed with the chemical potential construction (5), and an appropriate choice of the chemical free–energy.

We are left with two properties to be satisfied by the chemical free–energy to obtain a consistent model. First, the chemical free–energy of a two–phase system (when one of the phases is not present in the flow, e.g. phase three) is,

$$F_0^{[\boldsymbol{\sigma}]}(c_1, c_2, 0) = F_0^{\sigma_{12}}(c_1, c_2) = \sigma_{12} c_1^2 c_2^2. \tag{12}$$

A consistent chemical free–energy must satisfy that if one of the phases is not present, the resulting chemical free–energy is equivalent to that of a two–phase

flow for the other two fluids. A natural approach that satisfies this property is to add the chemical free–energies for the three possible pairs,

$$
\begin{aligned}
F_{0,NC}^{\sigma} &= F_0^{\sigma_{12}}(c_1, c_2) + F_0^{\sigma_{13}}(c_1, c_3) + F_0^{\sigma_{23}}(c_2, c_3) \\
&= \sigma_{12} c_1^2 c_2^2 + \sigma_{13} c_1^2 c_3^2 + \sigma_{23} c_2^2 c_3^2 .
\end{aligned}
\tag{13}
$$

Second, the reduction to a two–phase chemical free–energy is not enough to guarantee the consistency of the model. If $c_3(\mathbf{x}, 0) = 0$, then, to ensure $c_{3,t} = 0$, the chemical potential μ_3 must be algebraically zero. This implies that the chemical free–energy must satisfy that

$$
\left(\frac{1}{\Sigma_1} + \frac{1}{\Sigma_2} \right) \frac{\partial F_0^{\boldsymbol{\sigma}}}{\partial c_3} - \frac{1}{\Sigma_1} \frac{\partial F_0^{\boldsymbol{\sigma}}}{\partial c_1} - \frac{1}{\Sigma_2} \frac{\partial F_0^{\boldsymbol{\sigma}}}{\partial c_2} = 0, \quad \text{if } c_3 = 0.
\tag{14}
$$

Eq. (14) is automatically satisfied if an additional term is added to the inconsistent chemical free–energy (13),

$$
\begin{aligned}
F_0^{[\boldsymbol{\sigma}]} &= F_{0,NC}^{[\boldsymbol{\sigma}]} + c_1 c_2 c_3 \left(\Sigma_1 c_1 + \Sigma_2 c_2 + \Sigma_3 c_3 \right) \\
&= \sigma_{12} c_1^2 c_2^2 + \sigma_{13} c_1^2 c_3^2 + \sigma_{23} c_2^2 c_3^2 + c_1 c_2 c_3 \left(\Sigma_1 c_1 + \Sigma_2 c_2 + \Sigma_3 c_3 \right).
\end{aligned}
\tag{15}
$$

The chemical free–energy (15) completes the three–phase model. Note that this additional term also cancels when one of the phases is not present, and the chemical free–energy still reduces to that of a two–phase model (12). As a result, one Cahn–Hilliard equation (4) per phase is solved, with the chemical potential defined in (5) and the chemical free–energy in (15). In practice, since (7) holds, we only solve two Cahn–Hilliard equations (4), and the concentration of the third phase is obtained from the constraint (1), $c_3 = 1 - c_1 - c_2$. Its associated chemical potential, if needed, is also computed from the other two phases using (10).

2.1 Boundary conditions

The Cahn–Hilliard equation is complemented with an appropriate choice of the boundary conditions. Here we adopt a wall boundary condition model with non–zero contact angle for the three–phase Cahn–Hilliard equations.

Since the equation is fourth order in space, two boundary conditions must be specified, for both the chemical potentials and the concentration [4, 5]. To guarantee the phases conservation, we enforce a homogeneous Neumann boundary condition for the chemical potential,

$$
\nabla \mu_i \cdot \mathbf{n} \bigg|_{\partial \Omega} = 0.
\tag{16}
$$

For two–phase flows, a wall boundary condition with contact angle can be found in [46]. The latter is achieved with a non–homogeneous Neumann boundary condition for the concentration,

$$
\begin{aligned}
\nabla c_1 \cdot \mathbf{n} \Big|_{\partial \Omega} &= -\frac{4}{\varepsilon} \cos \theta_{12}^w c_1 c_2, \\
\nabla c_2 \cdot \mathbf{n} \Big|_{\partial \Omega} &= -\frac{4}{\varepsilon} \cos \theta_{21}^w c_1 c_2 = \frac{4}{\varepsilon} \cos \theta_{12}^w c_1 c_2.
\end{aligned}
\tag{17}
$$

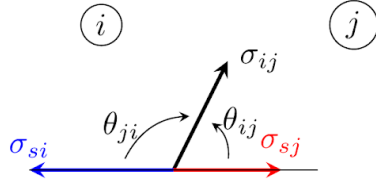The contact angle convention is represented in Fig. 1, such that θ_{ij} represents

Fig. 1 Convention used to designate the wall contact angle with respect to two phases i and j. Note that $\theta_{ij} + \theta_{ji} = \pi$

the angle of an interface between fluids i and j with fluid j, and θ_{ji} is that with fluid i. The relation between both angles that was applied in (17) is $\theta_{ij} + \theta_{ji} = \pi$. The stress equilibrium at the wall contact point implies that,

$$
\sigma_{si} = \sigma_{sj} + \sigma_{ij} \cos \theta_{ij}^w.
\tag{18}
$$

For three–phase flows, one can not choose freely the three contact angles with the wall, since a constraint relates them. We write the three wall stress equilibrium equations,

$$
\begin{aligned}
\sigma_{s1} &= \sigma_{s2} + \sigma_{12} \cos \theta_{12}^w, \\
\sigma_{s1} &= \sigma_{s3} + \sigma_{13} \cos \theta_{13}^w, \\
\sigma_{s2} &= \sigma_{s3} + \sigma_{23} \cos \theta_{23}^w.
\end{aligned}
\tag{19}
$$

Now we subtract the second equation to the first, and then add the third equation to the result, to find that wall contact angles and interface tension coefficients are constrained by the relation

$$
\sigma_{12} \cos \theta_{12}^w + \sigma_{23} \cos \theta_{23}^w = \sigma_{13} \cos \theta_{13}^w.
\tag{20}
$$

Lastly, in [47, 11] the non–homogeneous Neumann boundary condition was extended to three phases preserving the consistency property,

$$\nabla c_1 \cdot \mathbf{n}\Big|_{\partial\Omega} = -\frac{4}{\varepsilon}\left[\cos\theta_{12}^w c_1 c_2 (c_1 + c_2) + \cos\theta_{13}^w c_1 c_3 (c_1 + c_3)\right],$$

$$\nabla c_2 \cdot \mathbf{n}\Big|_{\partial\Omega} = -\frac{4}{\varepsilon}\left[-\cos\theta_{12}^w c_1 c_2 (c_1 + c_2) + \cos\theta_{23}^w c_2 c_3 (c_2 + c_3)\right], \qquad (21)$$

$$\nabla c_3 \cdot \mathbf{n}\Big|_{\partial\Omega} = \frac{4}{\varepsilon}\left[\cos\theta_{13}^w c_1 c_3 (c_1 + c_3) + \cos\theta_{23}^w c_2 c_3 (c_2 + c_3)\right].$$

Eq. (21) allows us to conveniently set the wall equilibrium contact angles.

3 Discontinuous Galerkin approximation

In this section we present a novel high–order discontinuous Galerkin approximation of the model presented in [18]. Among the different advantages of the DG method, exploited in this work, we highlight the capability to construct numerical approximations with arbitrarily high order of accuracy and the use of curvilinear elements in unstructured meshes to represent complex geometries.

3.1 Approximation and differential geometry

The physical domain Ω is tessellated with non–overlapping hexahedral elements. Then, we use a polynomial transfinite mapping to geometrically transform the elements to a reference element $E = [-1,1]^3$. The mapping relates physical ($\mathbf{x} = (x^1, x^2, x^3) = (x, y, z)$) and local ($\boldsymbol{\xi} = (\xi^1, \xi^2, \xi^3) = (\xi, \eta, \zeta)$) coordinates through a function $\mathbf{x} = \mathbf{X}(\boldsymbol{\xi})$. The details on how this function is constructed for a general curvilinear hexahedral can be found in [13].

The transfinite mapping is used to transform curvilinear elements to the reference element E. Associated to the transformation, we can compute the covariant and contravariant basis, and the Jacobian,

$$\mathbf{a}_i = \frac{\partial \mathbf{X}}{\partial \xi^i}, \;\; \mathbf{a}^i = \nabla\xi^i = \frac{1}{J}\mathbf{a}_j \times \mathbf{a}_k, \;\; J = \mathbf{a}_1 \cdot (\mathbf{a}_2 \times \mathbf{a}_3) \;\; i = 1, 2, 3, \;\; (i, j, k) \text{ cyclic.} \tag{22}$$

By construction, the contravariant basis satisfies the continuous metric identities, namely,

$$\sum_{i=1}^{3} \frac{\partial J a_n^i}{\partial \xi^i} = 0, \;\; n = 1, 2, 3. \tag{23}$$

The contravariant basis is also used to transform the differential operators involved in the equations. The gradient and divergence operators are, (see [33]),

$$\nabla u = \frac{1}{J}\boldsymbol{\mathcal{M}}\vec{\nabla}_\xi u, \quad \nabla \cdot \mathbf{f} = \frac{1}{J}\nabla_\xi \cdot \left(\boldsymbol{\mathcal{M}}^T \mathbf{f}\right) = \frac{1}{J}\nabla_\xi \cdot \tilde{\mathbf{f}}, \tag{24}$$

where $\nabla_\xi = (\partial/\partial\xi, \partial/\partial\eta, \partial/\partial\zeta)$, and $\boldsymbol{\mathcal{M}}$ is the metrics matrix,

$$\boldsymbol{\mathcal{M}} = \left(J\mathbf{a}^1, J\mathbf{a}^2, J\mathbf{a}^3\right). \tag{25}$$

Additionally, the product of a vector $\mathbf{f}$ by the transpose of the metrics matrix $\boldsymbol{\mathcal{M}}$ is called a contravariant vector, $\tilde{\mathbf{f}}$.

In the reference element, E, the solution is represented by polynomials of degree N, using tensor product Lagrange interpolating polynomials, $l_j(\xi)$,

$$l_j(\xi) = \prod_{\substack{i=0 \\ i\neq j}}^{N} \frac{\xi - \xi_i}{\xi_j - \xi_i}, \quad j = 0, ..., N. \tag{26}$$

The Lagrange polynomials are written in a set of Gauss or Gauss–Lobatto points, $\{\xi_i\}_{i=0}^{N}$. With the definitions (24), we approximate the solution inside the reference element as,

$$u(\mathbf{x}, t)\Big|_E \approx U(\boldsymbol{\xi}, t) = \sum_{i,j,k=0}^{N} U_{ijk}(t)l_i(\xi)l_j(\eta)l_k(\zeta). \tag{27}$$

where the time–dependent nodal degrees of freedom are $U_{ijk}(t) = U(\xi_i, \eta_j, \zeta_k, t)$. The convention used in this work is to adopt lower cases for continuous solutions, and upper cases for the polynomial approximations. The approximation of the metrics is done differently to (27) to obtain a discrete version of the metric identities (23). Following [33], we compute the contravariant basis as,

$$\mathcal{J}a_n^i = -\hat{e}^i \cdot \nabla_\xi \times \mathcal{I}^N\left(X_l\nabla_\xi X_m\right), \quad i,n = 1,2,3, \quad (n,m,l) \text{ cyclic}, \tag{28}$$

where $\hat{e}^i$ is the unit vector along the i–th spatial direction.

We construct Gauss quadrature rules to approximate integrals inside the reference element. We define the inner product of F and G as their product integral in the reference element,

$$\langle F, G\rangle_E = \int_E FG\,\mathrm{d}\xi \approx \int_{E,N} FG\,\mathrm{d}\xi = \langle F, G\rangle_{E,N} = \sum_{ijk} w_{ijk}F_{ijk}G_{ijk}. \tag{29}$$

The numerical quadrature weights $w_{ijk} = w_i w_j w_k$ are computed from the one dimensional integrals of the Lagrange polynomials,

$$w_i = \int_{-1}^{1} l_i(\xi) \, \mathrm{d}\xi, \quad i = 0, ..., N. \tag{30}$$

The numerical quadrature exactly approximates the integral of degree $2N \pm 1$ polymomials (+1 for Gauss, -1 for Gauss–Lobatto). Therefore, since the Lagrange polymomials satisfy the cardinal property, $l_i(\xi_j) = \delta_{ij}$, they are discretely orthonormal in the reference element,

$$\int_{-1,N}^{1} l_i(\xi) \, l_j(\xi) \, \mathrm{d}\xi = w_i \delta_{ij}, \tag{31}$$

where δ_{ij} is the Kronecker delta.

Lastly, given the reference element, the associated surface integral of a contravariant vector $\tilde{\mathbf{f}} = \left(f^\xi, f^\eta, f^\zeta \right)$ extends to all six faces that define the element,

$$\int_{\partial E} \tilde{\mathbf{f}} \cdot \hat{n} \, \mathrm{d}S_\xi = \int_{S_{\eta\zeta}} f^\xi \, \mathrm{d}\eta \, \mathrm{d}\zeta \bigg|_{\xi=-1}^{\xi=1} + \int_{S_{\xi\zeta}} f^\eta \, \mathrm{d}\xi \, \mathrm{d}\zeta \bigg|_{\eta=-1}^{\eta=1} + \int_{S_{\xi\eta}} f^\zeta \, \mathrm{d}\xi \, \mathrm{d}\eta \bigg|_{\zeta=-1}^{\zeta=1}, \tag{32}$$

where $\hat{n}$ is the outward pointing normal vector to the six faces of the reference element, $\mathrm{d}S_\xi$ is the surface differential in reference space. The discrete approximation of surface integrals is computed using the quadrature rules in two dimensions,

$$\int_{\partial E,N} \tilde{\mathbf{f}} \cdot \hat{n} \, \mathrm{d}S_\xi = \int_{S_{\eta\zeta},N} f^\xi \, \mathrm{d}\eta \, \mathrm{d}\zeta \bigg|_{\xi=-1}^{\xi=1} + \int_{S_{\xi\zeta},N} f^\eta \, \mathrm{d}\xi \, \mathrm{d}\zeta \bigg|_{\eta=-1}^{\eta=1} + \int_{S_{\xi\eta},N} f^\zeta \, \mathrm{d}\xi \, \mathrm{d}\eta \bigg|_{\zeta=-1}^{\zeta=1},$$

$$= \sum_{j,k=0}^{N} w_{jk} f^\xi(\xi, \eta_j, \zeta_k) \bigg|_{\xi=-1}^{\xi=1} + \sum_{i,k=0}^{N} w_{ik} f^\eta(\xi_i, \eta, \zeta_k) \bigg|_{\eta=-1}^{\eta=1}$$

$$+ \sum_{i,j=0}^{N} w_{ij} f^\zeta(\xi_i, \eta_j, \zeta) \bigg|_{\zeta=-1}^{\zeta=1}. \tag{33}$$

We can represent surface integrals in both physical and reference space. The relation between physical and reference integration variables is,

$$\mathrm{d}S^i = |\mathbf{a}_j \times \mathbf{a}_k| \, \mathrm{d}\xi^j \, \mathrm{d}\xi^k = |J\mathbf{a}^i| \, \mathrm{d}\xi^j \, \mathrm{d}\xi^k = J_f^i \, \mathrm{d}S_\xi^i \tag{34}$$

where $i = 1, 2, 3$ and $J_f^i = |J\mathbf{a}^i|$ is the face Jacobian. Moreover, from the definition of contravariant fluxes we get,

$$\tilde{\mathbf{f}} \cdot \hat{n}^i \, \mathrm{d}S_\xi^i = \left(\mathcal{M}^T \mathbf{f} \right) \cdot \hat{n}^i \, \mathrm{d}S_\xi^i = \mathbf{f} \cdot J\mathbf{a}^i \, \mathrm{d}S_\xi^i = \mathbf{f} \cdot \mathbf{n} \, \mathrm{d}S. \tag{35}$$

Therefore, we can write,

$$\int_{\partial E, N} \tilde{\mathbf{f}} \cdot \hat{n} \, \mathrm{d}S_\xi = \int_{\partial e, N} \mathbf{f} \cdot \mathbf{n} \, \mathrm{d}S, \tag{36}$$

being e an element in physical coordinates, and E the reference element.

3.2 Discontinuous Galerkin approximation of the three–phase model

The Cahn–Hilliard equation is fourth order in space. Thus, to construct a DG approximation, we rewrite the two Cahn–Hilliard equations as a four equation system of first order equations per phase. To do so, we introduce the auxiliary variables $\mathbf{g}_{c,i} = \nabla c_i$ and $\mathbf{g}_{\mu,i} = \nabla \mu_i$ so that,

$$
\begin{aligned}
c_{i,t} &= \frac{M_0}{\Sigma_i} \nabla \cdot \mathbf{g}_{\mu,i}, \\
\mathbf{g}_{\mu,i} &= \nabla \mu_i, \\
\mu_i &= \frac{12}{\varepsilon} f_i(c_1, c_2, c_3) - \frac{3}{4} \Sigma_i \varepsilon \nabla \cdot \mathbf{g}_{c,i}, \\
\mathbf{g}_{c,i} &= \nabla c_i.
\end{aligned}
\tag{37}
$$

Recall that f_i was defined in (6). Next, we transform the gradient and divergence operators to the reference space using (24),

$$
\begin{aligned}
Jc_{i,t} &= \frac{M_0}{\Sigma_i} \nabla_\xi \cdot \tilde{\mathbf{g}}_{\mu,i}, \\
J\mathbf{g}_{\mu,i} &= \mathcal{M} \nabla_\xi \mu_i, \\
J\mu_i &= \frac{12}{\varepsilon} J f_i(c_1, c_2, c_3) - \frac{3}{4} \Sigma_i \varepsilon \nabla_\xi \cdot \tilde{\mathbf{g}}_{c,i}, \\
J\mathbf{g}_{c,i} &= \mathcal{M} \nabla_\xi c_i.
\end{aligned}
\tag{38}
$$

We construct one weak form for each of the four equations. To do so, we multiply by arbitrary order N polynomials, φ_i, and integrate in E,

$$
\begin{aligned}
\langle Jc_{i,t}, \varphi_c\rangle_E &= \frac{M_0}{\Sigma_i}\langle\nabla_\xi\cdot\tilde{\mathbf{g}}_{\mu,i}, \varphi_c\rangle_E,\\
\left\langle J\mathbf{g}_{\mu,i}, \boldsymbol{\varphi}_{g_\mu}\right\rangle_E &= \left\langle\boldsymbol{\mathcal{M}}\nabla_\xi\mu_i, \boldsymbol{\varphi}_{g_\mu}\right\rangle_E = \left\langle\nabla_\xi\mu_i, \tilde{\boldsymbol{\varphi}}_{g_\mu}\right\rangle_E,\\
\langle J\mu_i, \varphi_\mu\rangle_E &= \frac{12}{\varepsilon}\langle Jf_i, \varphi_\mu\rangle_E - \frac{3}{4}\Sigma_i\varepsilon\langle\nabla_\xi\cdot\tilde{\mathbf{g}}_{c,i}, \varphi_\mu\rangle_E,\\
\left\langle J\mathbf{g}_{c,i}, \boldsymbol{\varphi}_{g_c}\right\rangle_E &= \left\langle\boldsymbol{\mathcal{M}}\nabla_\xi c_i, \boldsymbol{\varphi}_{g_c}\right\rangle_E = \left\langle\nabla_\xi c_i, \tilde{\boldsymbol{\varphi}}_{g_c}\right\rangle_E.
\end{aligned}
\tag{39}
$$

Note that in the second and fourth equations we have moved the metrics matrix to the vector test function to obtain contravariant test functions. Finally, we apply integration-by-parts to all integrals containing differential operators, and write the resulting surface integrals in physical space using (36),

$$
\begin{aligned}
\langle Jc_{i,t}, \varphi_c\rangle_E &= \frac{M_0}{\Sigma_i}\left(\int_{\partial e}\varphi_c\mathbf{g}_{\mu,i}\cdot\mathbf{n}\,\mathrm{d}S - \langle\tilde{\mathbf{g}}_{\mu,i}, \nabla_\xi\varphi_c\rangle_E\right),\\
\left\langle J\mathbf{g}_{\mu,i}, \boldsymbol{\varphi}_{g_\mu}\right\rangle_E &= \int_{\partial e}\mu_i\boldsymbol{\varphi}_{g_\mu}\cdot\mathbf{n}\,\mathrm{d}S - \left\langle\mu_i, \nabla_\xi\cdot\tilde{\boldsymbol{\varphi}}_{g_\mu}\right\rangle_E,\\
\langle J\mu_i, \varphi_\mu\rangle_E &= \frac{12}{\varepsilon}\langle Jf_i, \varphi_\mu\rangle_E - \frac{3}{4}\Sigma_i\varepsilon\left(\int_{\partial e}\varphi_\mu\mathbf{g}_{c,i}\cdot\mathbf{n}\,\mathrm{d}S - \langle\tilde{\mathbf{g}}_{c,i}, \nabla_\xi\varphi_\mu\rangle_E\right),\\
\left\langle J\mathbf{g}_{c,i}, \boldsymbol{\varphi}_{g_c}\right\rangle_E &= \int_{\partial e}c_i\boldsymbol{\varphi}_{g_c}\cdot\mathbf{n}\,\mathrm{d}S - \left\langle c_i, \nabla_\xi\cdot\tilde{\boldsymbol{\varphi}}_{g_c}\right\rangle_E.
\end{aligned}
\tag{40}
$$

We introduce the polynomial approximation ansatz in (40). We replace continuous functions by the order N polynomials and the exact integrals by the quadrature rules (29) and (33),

$$
\begin{aligned}
\langle\mathcal{J}C_{i,t}, \varphi_c\rangle_{E,N} &= \frac{M_0}{\Sigma_i}\left(\int_{\partial e,N}\varphi_c\mathbf{G}_{\mu,i}^\star\cdot\mathbf{n}\,\mathrm{d}S - \langle\tilde{\mathbf{G}}_{\mu,i}, \nabla_\xi\varphi_c\rangle_{E,N}\right),\\
\left\langle\mathcal{J}\mathbf{G}_{\mu,i}, \boldsymbol{\varphi}_{g_\mu}\right\rangle_{E,N} &= \int_{\partial e,N}\mu_i^\star\boldsymbol{\varphi}_{g_\mu}\cdot\mathbf{n}\,\mathrm{d}S - \left\langle\mu_i, \nabla_\xi\cdot\tilde{\boldsymbol{\varphi}}_{G_\mu}\right\rangle_{E,N},\\
\langle\mathcal{J}\mu_i, \varphi_\mu\rangle_{E,N} &= \frac{12}{\varepsilon}\langle\mathcal{J}F_i, \varphi_\mu\rangle_{E,N} - \frac{3}{4}\Sigma_i\varepsilon\left(\int_{\partial e,N}\varphi_\mu\mathbf{G}_{c,i}^\star\cdot\mathbf{n}\,\mathrm{d}S - \langle\tilde{\mathbf{G}}_{c,i}, \nabla_\xi\varphi_\mu\rangle_{E,N}\right),\\
\left\langle\mathcal{J}\mathbf{G}_{c,i}, \boldsymbol{\varphi}_{g_c}\right\rangle_E &= \int_{\partial e,N}C_i^\star\boldsymbol{\varphi}_{g_c}\cdot\mathbf{n}\,\mathrm{d}S - \left\langle C_i, \nabla_\xi\cdot\tilde{\boldsymbol{\varphi}}_{g_c}\right\rangle_{E,N}.
\end{aligned}
\tag{41}
$$

Since no continuity requirements to the discrete solution have been imposed at the inter–element faces, the boundary integrals are not uniquely defined. Thus, we replace the solution at the inter–element boundaries by an unique

solution, represented with the star. The inter–element solution and fluxes are responsible for the coupling between adjacent elements and the enforcement of boundary condition at the physical boundaries. In this work, we use the symmetric interior penalty method (IP),

$$C_i^\star = \{\!\{C_i\}\!\}, \;\; \mathbf{G}_{c,i}^\star = \{\!\{\nabla C_i\}\!\} - \sigma\,[\![C_i]\!], \;\; \mu_i^\star = \{\!\{\mu_i\}\!\}, \;\; \mathbf{G}_{\mu,i}^\star = \{\!\{\nabla \mu_i\}\!\} - \sigma\,[\![\mu_i]\!],$$
(42)

where the gradients are locally computed using (24), σ is the penalty parameter computed with the estimation by [48],

$$\sigma = \frac{(N+1)(N+2)}{2}\max\left\{|\mathcal{J}_f|\{\!\{\mathcal{J}^{-1}\}\!\}\right\},$$
(43)

and the jump operator accounts the face normal vectors,

$$[\![u]\!] = u_L\mathbf{n}_L + u_R\mathbf{n}_R.$$
(44)

The evolution equation for the coefficients is obtained replacing the test function by the Lagrange polynomials $\varphi = l_i\,(\xi)\,l_j(\eta)l_k(\zeta)$.

3.3 Boundary conditions

The boundary conditions enforcement is performed through the numerical fluxes at the physical boundaries. For the chemical potential gradient, we use a homogeneous Neumann boundary condition. Thus, the chemical potential is taken from the interior element, and the normal gradient is set to zero,

$$\mu_i^\star = \mu_i, \;\; \mathbf{G}_{\mu,i}^\star \cdot \mathbf{n} = 0, \;\; \text{in } \partial e \cap \partial \Omega.$$
(45)

For the concentration, we apply the non–homogeneous Neumann boundary condition that accounts for arbitrary wall contact angle (21). Thus, we use the interior value for the concentration, and the normal gradients are set to,

$$C_i^\star = C_i,$$
$$\mathbf{G}_{c,1}^\star \cdot \vec{n} = -\frac{4}{\varepsilon}\left(\cos\theta_{12}^w C_1 C_2\,(C_1 + C_2) + \cos\theta_{13}^w C_1\,(1 - C_1 - C_2)\,(1 - C_2)\right),$$
$$\mathbf{G}_{c,2}^\star \cdot \vec{n} = -\frac{4}{\varepsilon}\left(-\cos\theta_{12}^w C_1 C_2\,(C_1 + C_2) + \cos\theta_{23}^w C_2\,(1 - C_1 - C_2)\,(1 - C_1)\right).$$
(46)

As in the continuous boundary condition, the wall contact angles θ_{ij}^w are subjected to the constitutive constraint (20).

3.4 Time discretization

The semi–discrete scheme (41) is complemented with the numerical integration of the left hand side time derivative coefficients. Looking at the continuous equation (4), with chemical potential (5), one finds a linear bi–Laplacian operator for the concentration c_i, and a non–linear Laplacian term corresponding to the chemical free–energy derivatives. The bi–Laplacian operator involves fourth order derivatives, which translates in a severe numerical stiffness that restricts the time–step size in explicit solvers. Since the bi–Laplacian operator is linear, but the Laplacian of the chemical potential is non–linear, a commonly adopted technique is to use an IMplicit–EXplicit (IMEX) method [20, 13, 14].

We revisit the continuous setting (4)

$$c_{i,t} = M_0 \nabla^2 \left(\frac{12}{\Sigma_i \varepsilon} f_i - \frac{3}{4} \varepsilon \nabla^2 c_i \right) \tag{47}$$

to describe the approximation in time. We use the IMEX version of the first order Euler method described in [20]. We define the coefficients $c^n = c(t_n)$ as the solution evaluated in t_n, such that we evaluate the chemical free–energy in the old time step, t_n, and the interfacial energy in the new time step, t_{n+1},

$$\frac{c_i^{n+1} - c_i^n}{\Delta t} = M_0 \nabla^2 \left(\frac{12}{\Sigma_i \varepsilon} f_i(c_1^n, c_2^n, c_3^n) + S_0 \left(c_i^{n+1} - c_i^n \right) - \frac{3}{4} \nabla^2 c_i^{n+1} \right). \tag{48}$$

The term $S_0 \left(c_i^{n+1} - c_i^n \right)$ stabilizes the non–linear terms, where S_0 is a positive constant, while retaining first order accuracy. Note that the addition of the stabilization term modifies the Jacobian of the implicit solver, but maintains the linearity in c_i^{n+1}. Note that this implementation has two advantages:

1. The implicit system is decoupled: for each of the two phases, an individual linear system only involving c_i^{n+1} is solved.
2. The Jacobian matrix of the implicit solver is identical for the two phases. Hence, only one Jacobian matrix needs to be computed and stored. This matrix is constant in time due to the linearity.

In this work, the linear system of equations is solved with an LU factorization and Gauss substitution. Since the Jacobian matrix is constant in time, and the LU factorization is done only one time at the beginning of the computations. However, the algorithm does not restrict to other techniques, e.g. iterative solvers.

Finally, we introduce the IMEX scheme (48) in the semi–discrete DG formulation (41). To do so, in the definition of the chemical potential (the third equation of (41)), we evaluate the chemical free–energy t_n, the interfacial en-

ergy in t_{n+1}, and we add the dissipative term $S_0\left(C_i^{n+1} - C_i^n\right)$. As a result, the chemical potential is evaluated in a mixed IMEX state, which we call μ^θ, used to evaluate the rest of the variable. We get the fully–discrete system,

$$
\left\langle \mathcal{J}\frac{C_i^{n+1} - C_i^n}{\Delta t}, \varphi_c \right\rangle_{E,N} = \frac{M_0}{\Sigma_i}\left(\int_{\partial e,N} \varphi_c \mathbf{G}_{\mu,i}^{\star,\theta} \cdot \mathbf{n}\,\mathrm{d}S - \left\langle \tilde{\mathbf{G}}_{\mu,i}^\theta, \nabla_\xi \varphi_c \right\rangle_{E,N}\right),
$$

$$
\left\langle \mathcal{J}\mathbf{G}_{\mu,i}^\theta, \boldsymbol{\varphi}_{g_\mu} \right\rangle_{E,N} = \int_{\partial e,N} \mu_i^{\star,\theta} \boldsymbol{\varphi}_{g_\mu} \cdot \mathbf{n}\,\mathrm{d}S - \left\langle \mu_i^\theta, \nabla_\xi \cdot \tilde{\boldsymbol{\varphi}}_{G_\mu} \right\rangle_{E,N},
$$

$$
\left\langle \mathcal{J}\mu_i^\theta, \varphi_\mu \right\rangle_{E,N} = \frac{12}{\varepsilon}\left\langle \mathcal{J}F_i^n + S_0\left(C_i^{n+1} - C_i^n\right), \varphi_\mu \right\rangle_{E,N},
$$

$$
-\frac{3}{4}\Sigma_i \varepsilon \left(\int_{\partial e,N} \varphi_\mu \mathbf{G}_{c,i}^{\star,n+1} \cdot \mathbf{n}\,\mathrm{d}S - \left\langle \tilde{\mathbf{G}}_{c,i}^{n+1}, \nabla_\xi \varphi_\mu \right\rangle_{E,N}\right),
$$

$$
\left\langle \mathcal{J}\mathbf{G}_{c,i}^{n+1}, \boldsymbol{\varphi}_{g_c} \right\rangle_E = \int_{\partial e} C_i^{\star,n+1} \boldsymbol{\varphi}_{g_c} \cdot \mathbf{n}\,\mathrm{d}S - \left\langle C_i^{n+1}, \nabla_\xi \cdot \tilde{\boldsymbol{\varphi}}_{g_c} \right\rangle_{E,N}.
$$

$$(49)$$

The interested reader can find more details in [20, 13].

4 Numerical experiments

In this section we perform numerical experiments to evaluate the scheme presented and its numerical implementation. We first study the accuracy of the scheme with a convergence analysis, which solves a manufactured solution. Then, we study the captive bubble test, where a bubble is immersed between the two other phases. Lastly, we test the wall contact angle boundary condition solving two bubbles of two different phases immersed in the third phase.

4.1 Convergence analysis

We perform a two–dimensional convergence analysis based on the manufactured solution used in [20] to solve four phase flows,

$$
c_{1,m}(x,y;t) = \frac{1}{3}\left(1 + \cos\left(4\pi x\right)\sin\left(4\pi y\right)\sin\left(t\right)\right),
$$

$$
c_{2,m}(x,y;t) = \frac{1}{3}\left(1 + \cos\left(4\pi x\right)\sin\left(4\pi y\right)\sin\left(1.2t\right)\right),
$$

$$(50)$$

with the physical parameters given in Table 1. The physical domain is $\Omega = [-1,1]^2$, and we enforce periodic boundary conditions at the four physical boundaries. We solve the fully–discrete system (49) in a uniform Cartesian 2^2

Table 1 List of the parameter values used with the manufactured solution (50)

σ_{12}	σ_{13}	σ_{23}	M_0	ε	S_0	Δt
6.236E-3	7.265E-3	8.165E-3	1.0E-3	0.1	0.0	1.0E-4

grid until a final time $t_F = 0.1$, to then measure the L^2 errors as,

$$\|c_i - c_{i,m}\| = \sqrt{\sum_e \sum_{i,j,k=0}^{N} w_{ijk} \mathcal{J}_{ijk} \left(C_i - C_{i,m} \right)^2}. \qquad (51)$$

The L^2 errors for both fluids concentration are represented in Fig. 2. The
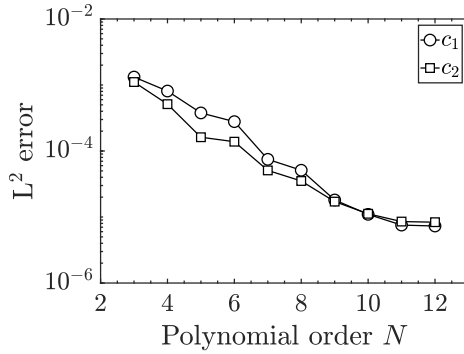
Fig. 2 Convergence study: L^2 errors as a function of the polynomial order N for the manufactured solution (50)

polynomial order ranges from $N = 3$ to $N = 12$. The error configuration is the typical: a region with under–resolution in space ($N < 11$) where the solution converges as the polynomial order increases, and a region with under–resolution in time ($N > 11$), where the error stagnates. We see that the error is higher for c_1 than for c_2, and that the behavior is not regular, with systematically higher convergence rates for odd polynomial orders. We see that for c_2, odd polynomial orders yield smaller errors than the theoretical linear behavior, while for c_1, on the contrary, even polynomial orders yield higher errors than expected. We do not have an answer for this behavior, although it has been seen in other works that particular choices of the manufactured solution might lead to this even–odd phenomena [49, 37, 13].

4.2 Captive bubble simulation

In the second test, we study a bubble (of phase 3) immersed in two layers of the other two phases. As a result of the interface tension, the equilibrium is reached when the angles between the different phases at the triple point $(c_1 = c_2 = c_3 = 1/3)$ satisfy [18],

$$\frac{\sigma_{23}}{\cos\theta_1} = \frac{\sigma_{13}}{\cos\theta_2} = \frac{\sigma_{12}}{\cos\theta_3}. \tag{52}$$

We consider the three different cases for the interface tension coefficients described in [18], which are summarized in Table 2 along with the equilibrium triple point angles computed with (52). For all the three cases, the initial

Table 2 Captive bubble simulation: interface tension coefficient values and equilibrium angles studied

Test	σ_{12}	σ_{13}	σ_{23}	θ_1	θ_2	θ_3
1	1	0.8	1.4	130.54°	111.80°	117.66°
2	1	1	1	120°	120°	120°
3	1	0.6	0.6	130.54°	111.80°	117.66°

condition is

$$c_1(x, y, 0) = \frac{1}{2}\left(1 + \tanh\left(\frac{2\min(\|\mathbf{x}\| - 0.1, y)}{\varepsilon}\right)\right),$$
$$c_2(x, y, 0) = \frac{1}{2}\left(1 - \tanh\left(\frac{2\max(0.1 - \|\mathbf{x}\|, y)}{\varepsilon}\right)\right), \tag{53}$$

which is represented in Fig. 3(a), where we have represented phase 1 in white, phase 2 in black, and phase 3 in gray. The domain is $\Omega = [-0.3, 0.3] \times [-0.15, 0.15]$, divided in a uniform Cartesian mesh with 40×20 elements, and we approximate the solution with $N = 8$ polynomials. We apply a wall boundary condition in all physical boundaries (with $\theta_{ij}^w = 90°$ wall contact angles). Recall that phase 1 is the upper layer represented in color white, phase 2 is the lower layer represented in color black, and the bubble is phase 3, colored in gray. The rest of the physical and numerical parameters are given in Table 3. The final equilibrium

Table 3 Captive bubble simulation: physical and numerical parameters

N	M_0	ε	S_0	Δt	θ_{12}^w	θ_{13}^w	θ_{23}^w
8	1.0E-4	0.01	8.0	0.01	90°	90°	90°

solution is represented in Fig. 3 for the three cases studied. In the first case

(a) Initial condition

(b) $\sigma_{12} = 1$, $\sigma_{13} = 0.8$, $\sigma_{23} = 1.4$

(c) $\sigma_{12} = 1$, $\sigma_{13} = 1$, $\sigma_{23} = 1$

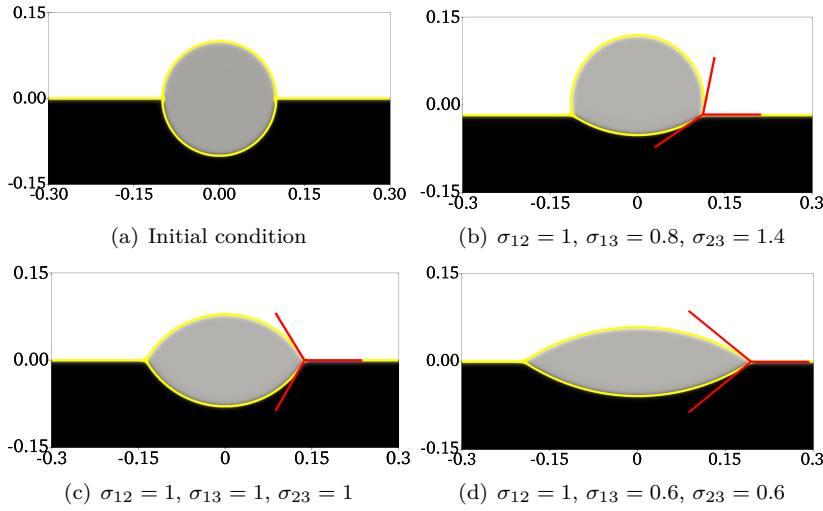(d) $\sigma_{12} = 1$, $\sigma_{13} = 0.6$, $\sigma_{23} = 0.6$

Fig. 3 Captive bubble simulation:

(Fig. 3(b)), given $\sigma_{13} < \sigma_{23}$, the bubble rises from the initial position, as a result of a higher interfacial tension of the bubble with phase 2 than compared with phase 1. In the other two cases (Figs. 3(c),3(d)), the conditions are symmetric as $\sigma_{13} = \sigma_{23}$, and we obtain a lenticular shape. We observe that when $\sigma_{12} > \sigma_{13} = \sigma_{23}$, the lens flattens. These results are in agreement with those in [18]. Moreover, in the right triple point, we have represented with red lines the angles estimated from the theoretical equilibrium configuration (52). We confirm that all three solutions show a good agreement with the theory (52) and with the reference [18].

4.3 Wall contact angle simulation

The last two–dimensional test case assesses the exactness of the wall contact angle boundary condition (21). We consider two bubbles of phases 1 and 2 in contact with the inferior and immersed in phase 3. We specify the equilibrium wall contact angles θ_{13}^w and θ_{23}^w, and compute the remaining third angle θ_{12}^w from (20). We maintain the same domain and mesh (with polynomial order

$N = 8$) used for the captive bubble simulation. The new initial condition is

$$c_1(x, y, 0) = \frac{1}{2} - \frac{1}{2} \tanh \left(\frac{2 \left(\sqrt{(x + 0.05)^2 + (y + 0.15)^2} - 0.1 \right)}{\varepsilon} \right),$$

$$\hat{c}_2(x, y, 0) = \frac{1}{2} - \frac{1}{2} \tanh \left(\frac{2 \left(\sqrt{(x - 0.1)^2 + (y + 0.12)^2} - 0.1 \right)}{\varepsilon} \right), \quad (54)$$

$$c_2(x, y, 0) = \min \left(\hat{c}_2(x, y, 0), 1 - c_1(x, y, 0) \right),$$

represented in Fig. 4(a). The rest of the physical parameters are given in

(a) Initial condition

(b) $\theta_{12} = 138.59°$, $\theta_{13} = 120°$, $\theta_{23} = 60°$

(c) $\theta_{12} = 104.48°$, $\theta_{13} = 60°$, $\theta_{23} = 60°$ (d) $\theta_{12} = 75.52°$, $\theta_{13} = 120°$, $\theta_{23} = 120°$
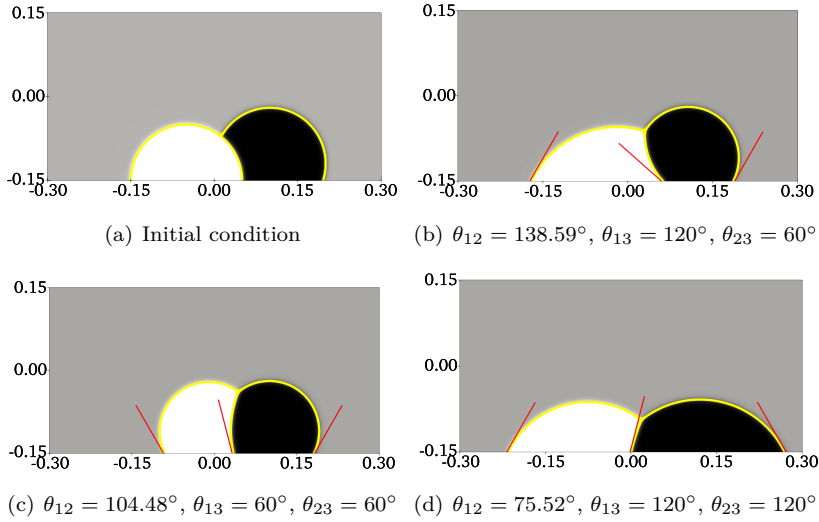
Fig. 4 Wall contact angle simulation

Table 4. We consider three different cases for the wall contact angles, given

Table 4 Wall contact angle simulation: physical and numerical parameters

M_0	ε	S_0	Δt	σ_{12}	σ_{13}	σ_{23}
1.0E-4	0.01	8.0	0.01	2.0	1.0	2.0

in Table 5, and such that each one results in a different configuration of the bubbles in equilibrium. The results are represented in Fig. 4. The red lines indicate the specified angles, following the convention described in Fig. 1. The first case, Fig. 4(b), represents a configuration where phase 1 is hydrophilic (wets the wall) and phase 2 is hydrophobic (rejects the wall). In the second case,

Table 5 Wall contact angle simulation: wall contact angles specified for the three tests studied

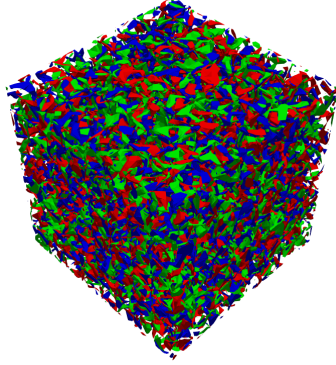| Test	θ_{12}^w	θ_{13}^w	θ_{23}^w
1	138.60°	120°	60°
2	104.48°	60°	60°
3	75.52°	120°	120°

Fig. 5 Spinodal decomposition in 3D cube: initial condition. The initial condition is computed from the random initialization (55) (blue is Phase 1, red is Phase 2, and green is Phase 3)

Fig. 4(c), both phases are hydrophobic, whereas in the third case, Fig. 4(c), both phases are hydrophilic. All in all, the contact angles with the wall are in agreement with those imposed by the boundary condition.

4.4 Spinodal decomposition in a three–dimensional cube

We now solve a spinodal decomposition in a three–dimensional cube $[-1, 1]^3$ with wall boundary conditions. The spinodal decomposition is the process of phase coarsening and growth from an initially mixed state. Therefore, we construct an initial condition for the three–phases from random values. In each point, we compute the phases as

$$c_i = \frac{r_i}{r_1 + r_2 + r_3}, \quad i = 1, 2, 3, \tag{55}$$

where r_i are random numbers in $[\frac{1}{3} - 0.3, \frac{1}{3} + 0.3]$. As a result, the conservation of phases (1) is satisfied, the average of each phase in the domain is close to $1/3$, and the range of each concentration is $[0.025, 0.905]$. We construct a uniform Cartesian mesh with $8 \times 8 \times 8$ elements, and we use a polynomial order $N = 5$. The random initial condition has been represented in Fig. 5.

Table 6 Spinodal decomposition in 3D cube: physical and numerical parameters

Test	N	M_0	ε	S_0	Δt	σ_{12}	σ_{13}	σ_{23}	θ_{12}^w	θ_{13}^w	θ_{23}^w
1	5	1.0	0.10	8.0	10^{-3}	1.0	1.0	1.0	$90°$	$90°$	$90°$
2	5	1.0	0.10	8.0	10^{-3}	1.0	1.0	1.0	$170°$	$90°$	$10°$

(a) $t = 0.02$ (b) $t = 0.1$ (c) $t = 0.2$

(d) $t = 0.5$ (e) $t = 1.0$ (f) $t = 10.0$
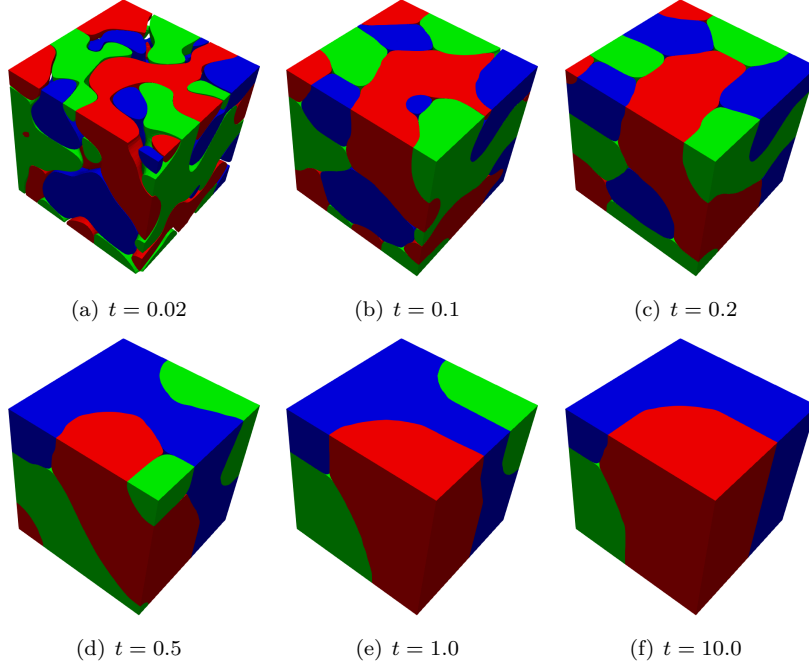
Fig. 6 Spinodal decomposition in a 3D cube, Test 1: evolution of the three phases (Phase 1 in blue, Phase 2 in red, Phase 3 in green). The phases evolve from the initial condition (Fig. 5) to reach a steady–state where the cube is divided in three big regions occupied by each of the phases

We solve the spinodal decomposition in two configurations. In Test 1, we use a neutral wall contact angle for the three phases, $\theta_{ij}^w = 90°$. Test 2 has $\theta_{12}^w = \theta_{32}^w = 10°$ between phases 1–2, and 3–2, keeping $\theta_{13}^w = 90°$ between phases 1–3. As a result, Phases 1 and 3 are hydrophilic and Phase 2 is hydrophobic. The rest of physical and numerical parameters are summarized in Table 6.

In Fig. 6, we represent the evolution of the three phases (Phase 1 in blue, Phase 2 in red, and Phase 3 in green) in Test 1. As time advances, we see that the phases coarsen and grow until a final equilibrium is reached. Since the walls are neutral in Test 1, the growth is spatially homogeneous between the three phases. Finally, a steady–state where the cube is divided in three regions is reached.
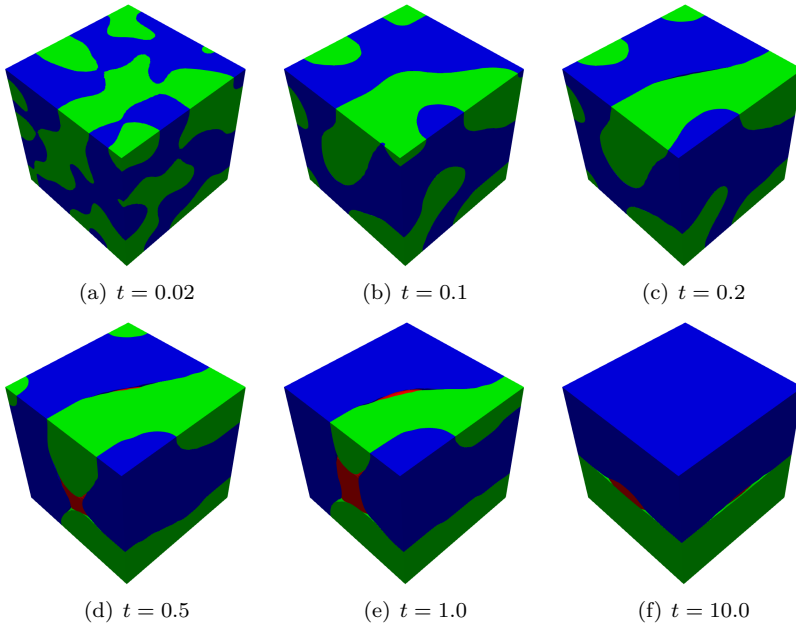
(a) $t = 0.02$ (b) $t = 0.1$ (c) $t = 0.2$

(d) $t = 0.5$ (e) $t = 1.0$ (f) $t = 10.0$

Fig. 7 Spinodal decomposition in 3D cube, Test 2: evolution of the three phases (Phase 1 in blue, Phase 2 in red, Phase 3 in green)

For Test 2, we represent the evolution of the three phases in Fig. 7, and the evolution of Phase 2 in Fig. 8. As Phase 2 is hydrophobic, in the early stages of the simulation Phase 2 grows only in the interior of the cube and at the boundary only Phases 1 and 3 are present. Then, as phase coarsening and growth follows, Phase 2 takes a form similar to an ellipsoid to minimize the surface tension, and its internal cavities are filled. In this process, Phase 2 ends having small contact with the walls. The final equilibrium is reached, where Phases 1 and 3 have divided the vast majority of the wall, and Phase 2 is confined to the interior of the cube, trapped between Phases 1 and 3 (similar to the captive bubble simulation).

Therefore, we conclude that wall affinity plays a crucial role on phase coarsening from mixture. In the initial stages, the growth is not homogeneous, as hydrophobic phases grow far from the wall. However, later on, to decrease surface tension in the interfaces, hydrophobic phases flatten their interfaces from the initial rounded form, at the expense of having contact with the wall.
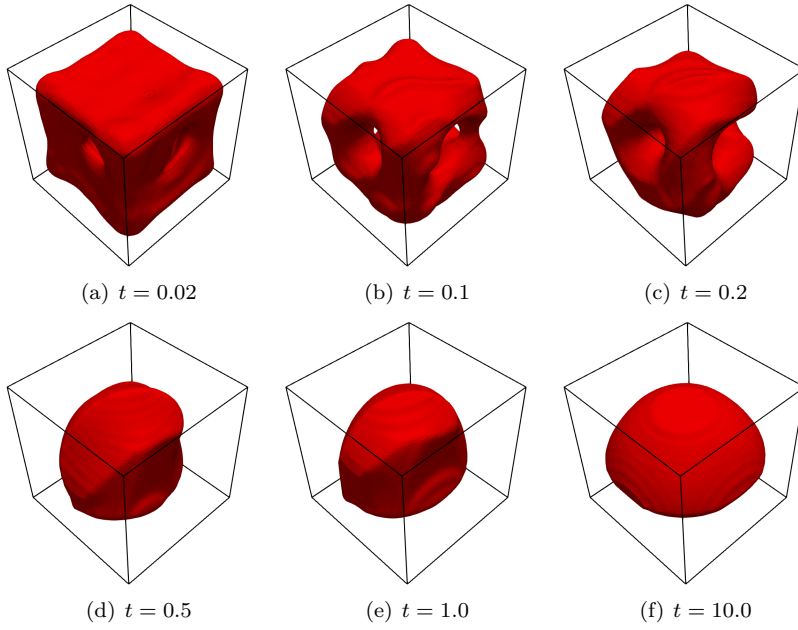
(a) $t = 0.02$ (b) $t = 0.1$ (c) $t = 0.2$

(d) $t = 0.5$ (e) $t = 1.0$ (f) $t = 10.0$

Fig. 8 Spinodal decomposition in 3D cube, Test 2: evolution of Phase 2. In the initial stages, Phase 2 grows far from the wall, approximately in a cubical geometry with internal cavities. Then, the cavities are filled and the shape evolves close to a sphere, still far from the wall. Finally, its surfaces flatten as a result of interfacial forces, at the expense of finally having small contacts with the walls

4.5 Spinodal decomposition in a three–dimensional pipe

Finally, we solve a spinodal decomposition in a T–pipe to show the geometrical flexibility allowed by the numerical method. Above the "T" junction, the domain features a straight upper section whose length is 3m, which is then coupled to a 90° bend whose radius is 3m. Additionally, on the right it has a straight 5m section, and then another 90°/3m bend. Finally, on the left it is coupled to a straight pipe whose length is 6m. The diameter of the pipe is $D = 1$m. The computational mesh used, with 1700 elements, is represented in Fig. 9. We perform two simulations with different wall contact angles: Test 1 has $\theta_{ij}^w = 90°$ wall contact angles between the three phases, whereas Test 2 has $\theta_{12}^w = \theta_{32}^w = 10°$ between phases 1–2, and 3–2, keeping $\theta_{13}^w = 90°$ between phases 1–3. Thus, Phases 1 and 3 are hydrophilic and Phase 2 is hydrophobic. The rest of the physical and numerical parameters are summarized in Table 7. We keep the random initial condition (55) represented in Fig. 10 for the pipe.
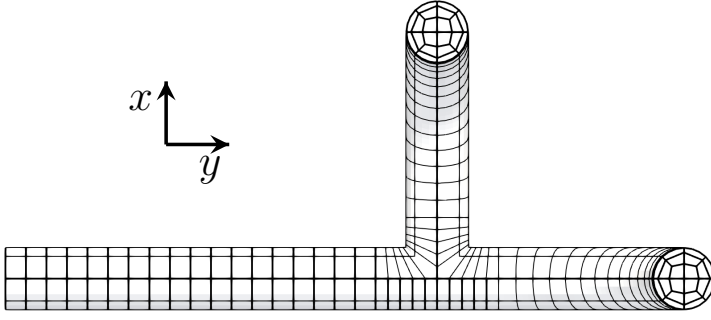
Fig. 9 Spinodal decomposition in 3D pipe: computational mesh for the T–pipe domain, with 1700 elements

Table 7 Spinodal decomposition in 3D pipe: physical and numerical parameters

Test	N	M_0	ε	S_0	Δt	σ_{12}	σ_{13}	σ_{23}	θ_{12}^w	θ_{13}^w	θ_{23}^w
1	4	1.0	0.15	8.0	10^{-3}	1.0	1.0	1.0	90°	90°	90°
2	4	1.0	0.15	8.0	10^{-3}	1.0	1.0	1.0	170°	90°	10°
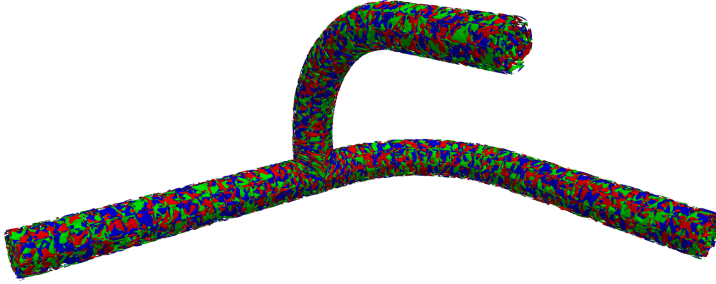
Fig. 10 Spinodal decomposition in 3D pipe: initial condition. The initial condition is computed from the random initialization (55) (blue is Phase 1, red is Phase 2, and green is Phase 3)

In Fig. 11 we have represented the evolution of the phases obtained in Test 1. From the initially mixed state, the phases coalesce and grow until an equilibrium is reached. In the three–dimensional pipe, the final configuration consists in a distribution of pipe slices completely filled with one of the three–phases. As the wall contact angle is 90° for all the three phases, they coalesce and grow homogeneously all across the pipe. Differently to the cube, in the pipe there are no triple points.

Finally, we solve Test 2. In Fig. 12 we have represented six snapshots of the three phases, and in Fig. 13 we have only represented Phase 2. As Phase 2
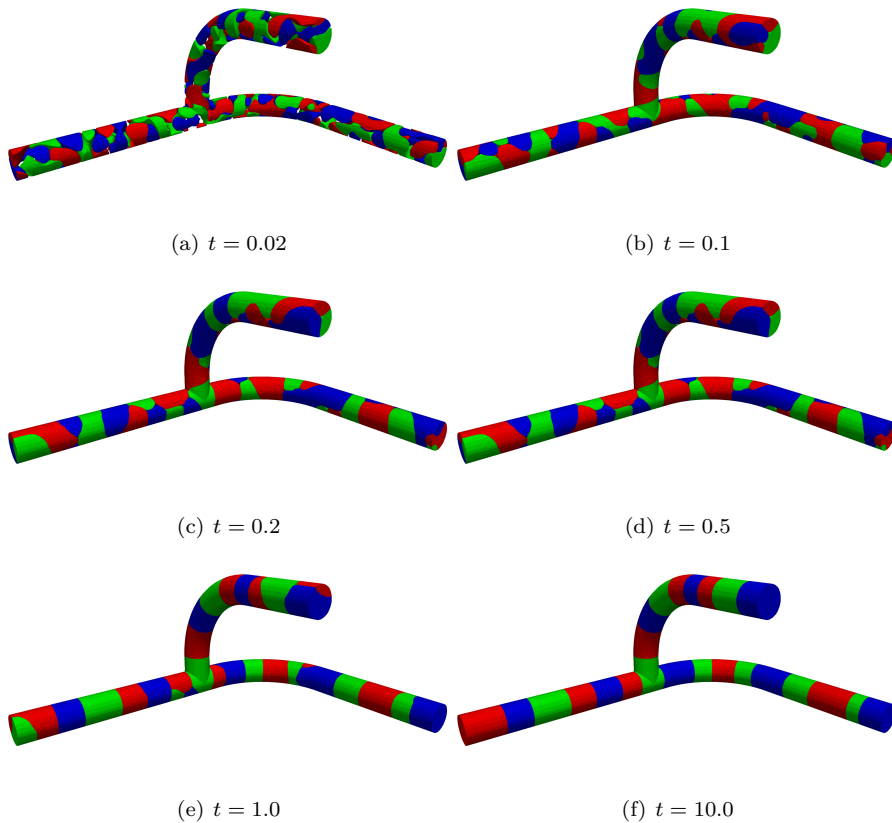
(a) $t = 0.02$ (b) $t = 0.1$

(c) $t = 0.2$ (d) $t = 0.5$

(e) $t = 1.0$ (f) $t = 10.0$

Fig. 11 Spinodal decomposition in a 3D pipe, Test 1: evolution of the three phases (Phase 1 in blue, Phase 2 in red, Phase 3 in green)

is hydrophobic, in the initial stages only Phases 1 and 3 grow near the wall, being Phase 2 confined to the pipe centerline. Then, interfacial forces tend to reduce the total area of Phase 2, which spreads to the rest of the pipe. In the final time, the pipe is filled with slices of the phases, except two sections, which are divided diametrally between Phases 1 and 3.

5 Conclusions

In this work, we have developed and implemented a high–order DG scheme for a three–phase Cahn–Hilliard model. The model developed in [18], complemented with the wall boundary condition developed in [21] (that allows the prescription of the wall contact angle for each of the three phases) has been chosen. The continuous system of equations is approximated with a discon-
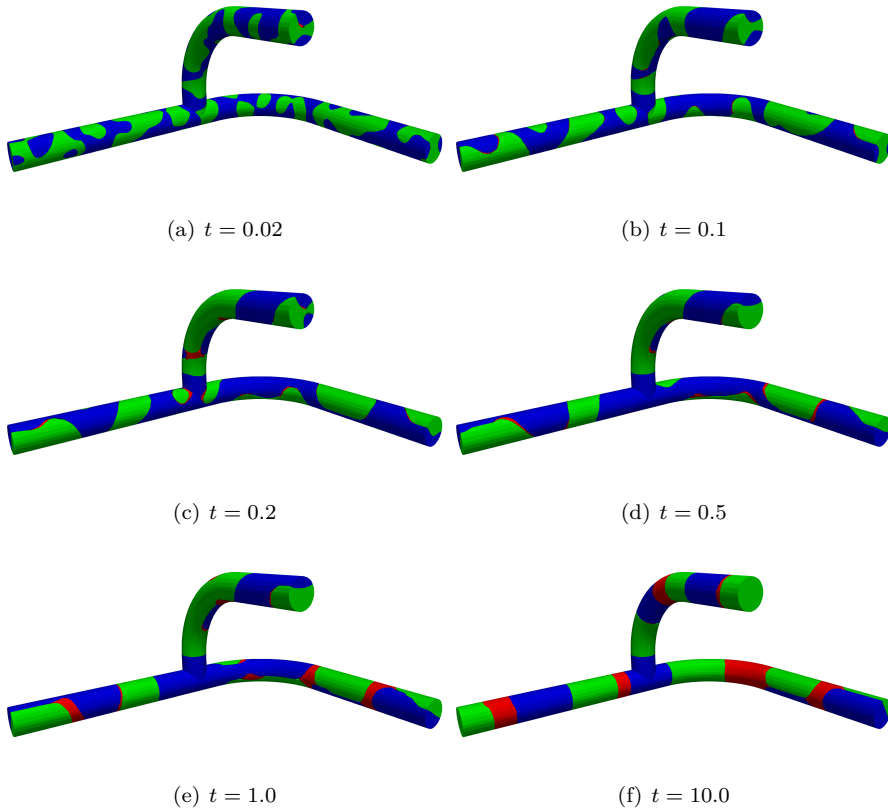
(a) $t = 0.02$

(b) $t = 0.1$

(c) $t = 0.2$

(d) $t = 0.5$

(e) $t = 1.0$

(f) $t = 10.0$

Fig. 12 Spinodal decomposition in 3D pipe, Test 2: evolution of the three phases (Phase 1 in blue, Phase 2 in red, Phase 3 in green). In the initial stages, only Phases 1 and 3 grow having contact with the walls, being Phase 2 confined to the interior. Then, as phases coalesce and grow, Phase 2 reduces its interfacial tension by completely filling pipe slices, similarly to Phases 1 and 3

tinuous Galerkin spectral element scheme (DGSEM) that uses the symmetric interior penalty method to compute the diffusive fluxes. We select a first order IMplicit–EXplicit (IMEX) method to integrate in time, such that non–linear terms are solved explicitly, whilst linear terms are solved implicitly. The solution of the fully–discrete system involves the solution of one linear system for each of the Cahn–Hilliard equations. The two linear systems, however, are decoupled and such that the Jacobian matrices are constant in time and identical for both Cahn–Hilliard equations. With this method, only one Jacobian matrix is needed and only one LU factorization is performed for the two equations. Finally, two and three–dimensional numerical experiments have been performed to evaluate the scheme presented and its numerical implementa-
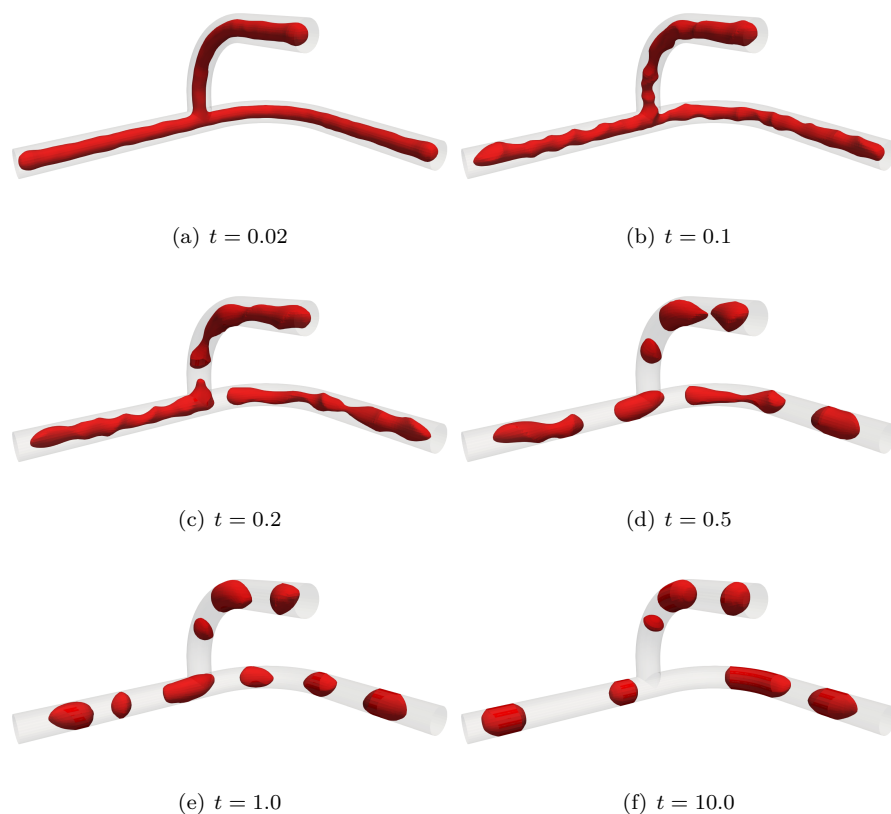
(a) $t = 0.02$ (b) $t = 0.1$

(c) $t = 0.2$ (d) $t = 0.5$

(e) $t = 1.0$ (f) $t = 10.0$

Fig. 13 Spinodal decomposition in 3D pipe, Test 2: evolution of Phase 2. Initially, Phase 2 is confined to the interior of the pipe, whereas Phases 1 and 3 grow at the surface. Then, to decrease the interfacial energy, it breaks into smaller pieces with rounded shape. Finally, it entirely occupies several pipe slices. However, at the interfaces with Phases 1 and 3 the shapes are rounded to keep the imposed wall contact angle

tion. The method presents spectral convergence and correctly reproduces the contact angles between the different phases (both in the bulk and in the wall).

References

1. M. Sussman, P. Smereka, S. Osher, A level set approach for computing solutions to incompressible two-phase flow, Journal of Computational physics 114 (1) (1994) 146–159 (1994).

2. D. Adalsteinsson, J. A. Sethian, A fast level set method for propagating interfaces, Journal of computational physics 118 (2) (1995) 269–277 (1995).

3. S. Van der Pijl, A. Segal, C. Vuik, P. Wesseling, A mass-conserving level-set method for modelling of multi-phase flows, International journal for numerical methods in fluids 47 (4) (2005) 339–361 (2005).

4. J. W. Cahn, J. E. Hilliard, Free energy of a nonuniform system. I. Interfacial free energy, The Journal of chemical physics 28 (2) (1958) 258–267 (1958).

5. J. W. Cahn, J. E. Hilliard, Free energy of a nonuniform system. III. Nucleation in a two-component incompressible fluid, The Journal of chemical physics 31 (3) (1959) 688–699 (1959).

6. C. M. Elliott, H. Garcke, On the Cahn–Hilliard equation with degenerate mobility, Siam journal on mathematical analysis 27 (2) (1996) 404–423 (1996).

7. J. Lowengrub, L. Truskinovsky, Quasi–incompressible Cahn–Hilliard fluids and topological transitions, Proceedings of the Royal Society of London. Series A: Mathematical, Physical and Engineering Sciences 454 (1978) (1998) 2617–2654 (1998).

8. H. Gómez, V. M. Calo, Y. Bazilevs, T. J. Hughes, Isogeometric analysis of the Cahn–Hilliard phase-field model, Computer methods in applied mechanics and engineering 197 (49-50) (2008) 4333–4352 (2008).

9. J. Shen, X. Yang, Numerical approximations of Allen-Cahn and Cahn-Hilliard equations, Discrete Contin. Dyn. Syst 28 (4) (2010) 1669–1691 (2010).

10. S. Dong, An efficient algorithm for incompressible N-phase flows, Journal of Computational Physics 276 (2014) 691–728 (2014).

11. S. Dong, Wall-bounded multiphase flows of N immiscible incompressible fluids: Consistency and contact-angle boundary condition, Journal of Computational Physics 338 (2017) 21–67 (2017).

12. S. Gómez-Álvarez, A. Rivero-Jiménez, G. Rubio, J. Manzanero, C. Redondo, et al., Novel Coupled Cahn-Hilliard Navier-Stokes Solver for the Evaluation of Oil and Gas Multiphase Flow, in: BHR 19th International Conference on Multiphase Production Technology, BHR Group, 2019 (2019).

13. J. Manzanero, G. Rubio, D. A. Kopriva, E. Ferrer, E. Valero, A free-energy stable nodal discontinuous Galerkin approximation with summation-by-parts property for the Cahn-Hilliard equation, Journal of Computational Physics 403 (2020) 109072 (2020).

14. J. Manzanero, G. Rubio, D. A. Kopriva, E. Ferrer, E. Valero, Entropy-stable discontinuous Galerkin approximation with summation-by-parts property for the incompressible Navier-Stokes/Cahn-Hilliard system, Journal of Computational Physics (2020) 109363 (2020).

15. J. Manzanero, C. Redondo, G. Rubio, E. Ferrer, E. Valero, S. Gómez-Álvarez, Á. Rivero, A high–order discontinuous Galerkin solver for multiphase flows, in: Spectral and High Order Methods for Partial Differential Equations ICOSAHOM 2018 (accepted), Springer, 2020 (2020).

16. Y. Xia, Y. Xu, C.-W. Shu, Application of the local discontinuous Galerkin method for the Allen-Cahn/Cahn-Hilliard system, Communications in Computational Physics 5 (2-4) (2009) 821–835 (2009).

17. J. Shen, X. Yang, Energy stable schemes for Cahn-Hilliard phase-field model of two-phase incompressible flows, Chinese Annals of Mathematics, Series B 31 (5) (2010) 743–758 (2010).

18. F. Boyer, C. Lapuerta, Study of a three component Cahn-Hilliard flow model, ESAIM: Mathematical Modelling and Numerical Analysis 40 (4) (2006) 653–687 (2006).

19. F. Boyer, S. Minjeaud, Hierarchy of consistent N-component Cahn–Hilliard systems, Mathematical Models and Methods in Applied Sciences 24 (14) (2014) 2885–2928 (2014).

20. S. Dong, Multiphase flows of N immiscible incompressible fluids: A reduction-consistent and thermodynamically-consistent formulation and associated algorithm, Journal of Computational Physics 361 (2018) 1–49 (2018).

21. Y. Shi, X.-P. Wang, Modeling and simulation of dynamics of three-component flows on solid surface, Japan Journal of Industrial and Applied Mathematics 31 (3) (2014) 611–631 (2014).

22. D.A. Kopriva, Implementing spectral methods for partial differential equations, Springer Netherlands, 2009 (2009).

23. M. F. Wheeler, An elliptic collocation-finite element method with interior penalties, SIAM Journal on Numerical Analysis 15 (1) (1978) 152–161 (1978).

24. E. Ferrer and R.H.J. Willden, A high order discontinuous Galerkin finite element solver for the incompressible Navier–Stokes equations, Computers & Fluids 46 (1) (2011) 224–230 (2011).

25. E. Ferrer and R. H.J. Willden, A high order discontinuous Galerkin - Fourier incompressible 3D Navier-Stokes solver with rotating sliding meshes, Journal of Computational Physics 231 (21) (2012) 7037–7056 (2012).

26. E. Ferrer, An interior penalty stabilised incompressible Discontinuous Galerkin - Fourier solver for implicit Large Eddy Simulations, Journal of Computational Physics 348 (2017) 754–775 (2017).

27. J. Manzanero, A. M. Rueda-Ramírez, G. Rubio, E. Ferrer, The Bassi Rebay 1 scheme is a special case of the symmetric interior penalty formulation for discontinuous Galerkin discretisations with Gauss–Lobatto points, Journal of Computational Physics 363 (2018) 1–10 (2018).

28. J. S. Hesthaven, T. Warburton, Nodal discontinuous Galerkin methods: algorithms, analysis, and applications, Springer Science & Business Media, 2007 (2007).

29. G. Gassner, D. A. Kopriva, A comparison of the dispersion and dissipation errors of Gauss and Gauss–Lobatto discontinuous Galerkin spectral element methods, SIAM Journal on Scientific Computing 33 (5) (2011) 2560–2579 (2011).

30. R. C. Moura, S. J. Sherwin, J. Peiró, Linear dispersion–diffusion analysis and its application to under-resolved turbulence simulations using discontinuous Galerkin spectral/hp methods, Journal of Computational Physics 298 (2015) 695–710 (2015).

31. J. Manzanero, G. Rubio, E. Ferrer, E. Valero, Dispersion-dissipation analysis for advection problems with nonconstant coefficients: Applications to discontinuous Galerkin formulations, SIAM Journal on Scientific Computing 40 (2) (2018) A747–A768 (2018).

32. J. Manzanero, E. Ferrer, G. Rubio, E. Valero, Design of a smagorinsky spectral vanishing viscosity turbulence model for discontinuous Galerkin methods, Computers & Fluids (2020) 104440 (2020).

33. D. A. Kopriva, Metric identities and the discontinuous spectral element method on curvilinear meshes, Journal of Scientific Computing 26 (3) (2006) 301 (2006).

34. M. Kompenhans, G. Rubio, E. Ferrer, and E. Valero, Comparisons of p–adaptation strategies based on truncation– and discretisation–errors for high order discontinuous Galerkin methods, Computers & Fluids 139 (2016) 36 – 46, 13th {USNCCM} International Symposium of High-Order Methods for Computational Fluid Dynamics - A special issue dedicated to the 60th birthday of Professor David Kopriva (2016).

35. M. Kompenhans, G. Rubio, E. Ferrer, and E. Valero, Adaptation strategies for high order discontinuous Galerkin methods based on tau-estimation, Journal of Computational Physics 306 (2016) 216 – 236 (2016).

36. A. M. Rueda-Ramírez, J. Manzanero, E. Ferrer, G. Rubio, E. Valero, A p-multigrid strategy with anisotropic p-adaptation based on truncation errors for high-order discontinuous Galerkin methods, Journal of Computational Physics 378 (2019) 209–233 (2019).

37. G. J. Gassner, A. R. Winters, D. A. Kopriva, Split form nodal discontinuous Galerkin schemes with summation-by-parts property for the compressible Euler equations, Journal of Computational Physics 327 (2016) 39–66 (2016).

38. A. R. Winters, G. J. Gassner, Affordable, entropy conserving and entropy stable flux functions for the ideal MHD equations, Journal of Computational Physics 304 (2016) 72–108 (2016).

39. J. Manzanero, G. Rubio, E. Ferrer, E. Valero, D. A. Kopriva, Insights on aliasing driven instabilities for advection equations with application to Gauss–Lobatto discontinuous Galerkin methods, Journal of Scientific Computing 75 (3) (2018) 1262–1281 (2018).

40. G. J. Gassner, A. R. Winters, F. J. Hindenlang, D. A. Kopriva, The BR1 scheme is stable for the compressible Navier–Stokes equations, Journal of Scientific Computing 77 (1) (2018) 154–200 (2018).

41. J. Manzanero, G. Rubio, D. A. Kopriva, E. Ferrer, E. Valero, An entropy–stable discontinuous Galerkin approximation for the incompressible Navier–Stokes equations with variable density and artificial compressibility, Journal of Computational Physics 408 (2020) 109241 (2020).

42. F. Fraysse, C. Redondo, G. Rubio, E. Valero, Upwind methods for the Baer–Nunziato equations and higher-order reconstruction using artificial viscosity, Journal of Computational Physics 326 (2016) 805–827 (2016).

43. C. Redondo, F. Fraysse, G. Rubio, E. Valero, Artificial Viscosity Discontinuous Galerkin Spectral Element Method for the Baer-Nunziato Equations, in: Spectral and High Order Methods for Partial Differential Equations ICOSAHOM 2016, Springer, 2017, pp. 613–625 (2017).

44. F. Boyer, S. Minjeaud, Numerical schemes for a three component Cahn-Hilliard model, ESAIM: Mathematical Modelling and Numerical Analysis 45 (4) (2011) 697–738 (2011).

45. Y. Xia, Y. Xu, C.-W. Shu, Local discontinuous Galerkin methods for the Cahn–Hilliard type equations, Journal of Computational Physics 227 (1) (2007) 472–491 (2007).

46. S. Dong, On imposing dynamic contact-angle boundary conditions for wall-bounded liquid–gas flows, Computer Methods in Applied Mechanics and Engineering 247 (2012) 179–200 (2012).

47. Y. Shi, X.-P. Wang, Modeling and simulation of dynamics of three-component flows on solid surface, Japan Journal of Industrial and Applied Mathematics 31 (3) (2014) 611–631 (2014).

48. K. Shahbazi, Short note: An explicit expression for the penalty parameter of the interior penalty method, Journal of Computational Physics 205 (2) (2005) 401–407 (May 2005).

49. G. Rubio, F. Fraysse, J. De Vicente, E. Valero, The estimation of truncation error by τ-estimation for Chebyshev spectral collocation method, Journal of Scientific Computing 57 (1) (2013) 146–173 (2013).